Bioinspired noncovalently crosslinked "fuzzy" carbon nanotube bundles with superior toughness and strength†

Graham H. Bratzel,[ab] Steven W. Cranford,[a] Horacio Espinosa[c] and Markus J. Buehler*[a]

Received 13th June 2010, Accepted 23rd August 2010
DOI: 10.1039/c0jm01877e

Carbon nanotubes (CNTs) constitute a prominent example of structural nanomaterials, with many potential applications that could take advantage of their unique mechanical properties. Utilizing the inherent strength of CNTs at larger length-scales is, however, hindered by the inherently weak intertube bonding interactions, allowing slippage of nanotubes within a bundle before large macroscopic stresses are reached. Many lamellar biological materials crosslink stiff fibrous components *via* the introduction of a soft binding matrix to achieve a combination of high strength and toughness, as seen in cellulosic wood, silk, or collagenous bone fibrils. Here we present atomistic-based multi-scale simulation studies of bundles of carbon nanotubes with the inclusion of a binding polymer (polyethylene chains with functional end groups) to demonstrate the control of mechanical properties *via* variations of polymer structure, content and fiber geometry. A hierarchical approach (coarse–grain molecular modelling) is implemented to develop a framework that can successfully integrate atomistic theory and simulations with material synthesis and physical experimentation, and facilitate the investigation of such novel bioinspired structural materials. Using two types of nanomechanical tests, we explore the effects of crosslink length and concentration on the ultimate tensile stress and modulus of toughness of a carbon nanotube bundle. We demonstrate that the ultimate tensile stress can be increased four-fold, and the modulus of toughness five-fold, over an uncrosslinked bundle with the inclusion of 1.5 nm long crosslinking polymer at 17 wt% concentration, providing the structural basis for a fibre material that combines high levels of stress at high levels of toughness. These noncovalently crosslinked carbon nanotube bundles exhibit residual strengths after initiation of failure that depend on the crosslink length, and are similar to plastically sheared wood cells. Our work demonstrates the implementation of a wood-inspired carbon nanotube based fibre material with superior mechanical properties.

1. Introduction

Carbon nanotubes (CNTs) are among the most widely studied nanomaterials, with many potential applications that take advantage of their unique mechanical, electrical, thermal, and optical properties.[1] The superior mechanical properties of CNTs are appealing for their potential use in novel nanomaterials, including the design of fibers. For instance, the Young's modulus of a single-walled nanotube approaches a terapascal (10^{12} Pa),[2] implying that CNTs are one of the strongest known synthesized materials in terms of their elastic modulus and ultimate tensile strength.[3] For over a decade, attempts have been made to utilize the high strength of individual CNTs in an efficient manner, but persistent challenges remain to bring about the superior properties of CNTs at the nanoscale to larger, macroscopic scales. The interaction of individual CNTs in larger-scale structures often plays a critical role in the mechanical properties of CNT systems. Thereby, the properties of bundles of CNTs are severely influenced by the detailed nanoscale geometry and by chemical elements that define the material nanostructure. At the nanoscale, weak van der Waals interactions govern the structural organization and the mechanical properties of CNT-based materials. For example, the high axial strength of individual nanotubes is lost when nanotubes form bundles as the weak vdW forces allow slippage of nanotubes within a bundle.[4,5] Such effects are also found in nanotube based fibres or ropes,[6,7] as well as in vertically aligned nanotube arrays.[8–10] The potential to reinforce bundles and yarns and to manipulate adhesive forces at the atomistic, molecular, and global material scales would have immediate effects in the applications of CNT systems to create macroscopically strong systems. For many applications, the beneficial mechanical properties of CNTs can only be harnessed if these properties are maintained at the larger length scales of long, continuous CNT nanofibers. Advancing our understanding of the structural arrangements and mechanisms resulting from intertube and polymer–tube interactions is necessary for the development of macroscopically functional materials and structures that take advantage of bundling nanotubes, such as CNT fibres implemented for composite reinforcement. While much work has focused on CNT–polymer composite in which

[a]*Laboratory for Atomistic and Molecular Mechanics, Department of Civil and Environmental Engineering, Massachusetts Institute of Technology, 77 Massachusetts Ave. Room 1-235A&B, Cambridge, MA, USA. Web: http://web.mit.edu/mbuehler/www/; E-mail: mbuehler@MIT.EDU; Fax: +1-617-324-4014; Tel: +1-617-452-2750*
[b]*Department of Mechanical Engineering, Massachusetts Institute of Technology, 77 Massachusetts Ave., Cambridge, MA, USA*
[c]*Department of Mechanical Engineering, Northwestern University, 2145 Sheridan Road, Evanston, IL, USA*
† This paper is part of a *Journal of Materials Chemistry* themed issue on Modelling of Materials. Guest editors: Julian Gale and Mark Wilson.

nanotubes reinforce a polymer matrix,[11–13] the study presented here investigates a nanofiber that is predominately CNT-based, in which a disordered polymer phase serves to enhance the adhesion of adjacent nanotubes.

This approach is based on the hypothesis that a possible strategy in overcoming the limitations of conventional engineered materials, specifically carbon-based composites, is the incorporation of hierarchical microstructures with defined levels of order and disorder, as found in biological materials like bone, wood, spider silk, and many others.[14] Bone, for example, achieves superior mechanical properties by crosslinking stiff but brittle mineral crystals with soft and tough collagen fibers, creating a hierarchical composite that is both strong and tough.[15] Wood derives its properties from a similarly organized nanocomposite, and shows that adaptability is another major factor in what sets biological materials apart from existing engineered materials. Adaptive mechanisms such as sacrificial bonds and bond reformation after plastic deformation allow wood to be such a strong building material as well as tough and resistant to catastrophic fracture when alive. When the stress is relaxed after wood cells are plastically sheared, sacrificial hydrogen bonds in the lignin matrix between the wood cells reform.[16] This maintains the capacity to undergo plastic deformation again, where wood then loads to the same stress level before plastically shearing. The lignin matrix is irreversibly elongated, but the strong cellulosic microfibrils that wrap the wood cells are not damaged. The microfibrils carry the majority of the load, while hydrogen bonds in the lignin matrix act as sacrificial energy-dissipation bonds in order to protect the wood cells. In order for this sacrifice to take place, there must be a strong binding between the crystalline cellulose microfibrils and the amorphous lignin. Hemicellulose is an amorphous form of the crystalline cellulose comprising the microfibrils and can bond well to both cellulose and lignin, as depicted in Fig. 1a, offering inspiration for a self-repair mechanism in bioinspired synthetic fiber materials. Recent work in this field has suggested that the general design paradigm in bioinspired materials is that the series of structures that emerge at different length-scales provide the structural basis for superior properties at the macroscale.

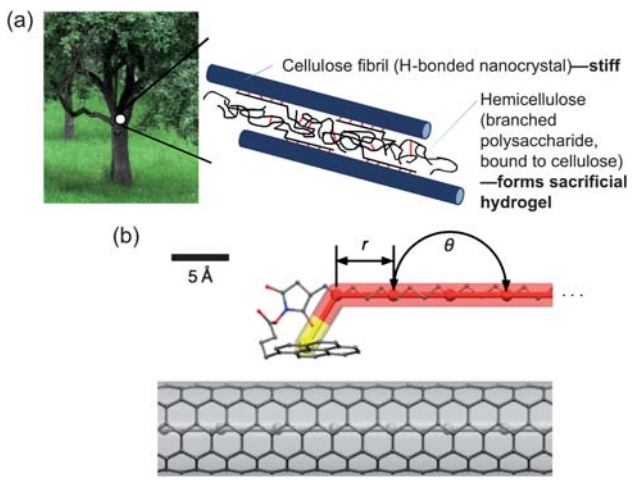

Fig. 1 Schematics of a wood fibril and the noncovalently crosslinked CNT bundle model. (a) Nanostructure of wood. Strong cellulose fibrils, H-bonded nanocrystals, wrap the wood cell and carry most of the load while soft, sacrificial hemicellulose and lignin between cells transfer load. (b) Wood's sacrificial hydrogel is mimicked here by terminating each end of a short, unbranching polyethylene chain with PSE in order to noncovalently adsorb polymer crosslinks to the CNT sidewall. The bead-spring model, superimposed to scale over the atomistic model, shows the computational advantage of coarse–grain techniques in the reduced number of particles, N, and the reduced number of parameters, *i.e.* spring length r and angle θ. A translucent representation shows the relative scale of other figures in this paper for comparison.

Supplementary to experimental synthesis efforts to create advanced CNT-based composites, bottom-up computational approaches can provide a powerful means to investigate potential carbon nanotube composite materials, indicating possible systems and configurations that warrant experimental and physical realization. Such approaches include quantum mechanics studies,[17,18] full atomistic molecular dynamics,[19] and coarse–grain models[20] that investigate the potential interaction between carbon nanotubes and various material interfaces. Here we utilize an atomistic based coarse–grain approach to investigate the structural and mechanical properties of biologically inspired CNT bundle systems. In this paper, we present an *in silico* model of a wood-inspired, noncovalently crosslinked, "fuzzy" CNT bundle, shown in Fig. 1b, that uses noncovalent sidewall adsorption to mimic the slip–stick shearing behavior of wood cells. We outline the details of this novel fiber material in the next section.

1.1 Functional sidewall adsorption

A traditional method of creating crosslinks within CNT bundles is to use an ion beam to knock carbon atoms out of the CNT sidewall to form short, covalent carbon-chain crosslinks between adjacent CNTs. These crosslinks greatly increase the bundle properties by preventing nanotube sliding: for example, a 30-fold increase in bending modulus has been achieved experimentally.[5] However, these crosslinks are brittle, break permanently, and introduce defects in the CNT sidewall, which in turn greatly reduce the very properties of individual CNTs that we try to exploit. Instead, the use of noncovalent sidewall adsorption can link adjacent as well as nonadjacent CNTs and does not damage the structural or electrical properties of the pristine CNT. The adsorption is inherently weaker than covalent functionalization, but can re-adsorb to other sidewall sites after large bundle deformation, similar to sheared wood cells. A related study[21] has shown that surfactant adsorption between close CNTs creates a stabilizing attractive force, offering the possibility for directed self-assembly.

For the present study, we choose crosslinks made of 1-Pyrenebutanoic Acid, Succinimidyl Ester (PSE) end-groups connected by ultra-short polyethylene chains. The aromatic pyrenyl group of PSE has been shown to adsorb to CNT sidewalls by noncovalent π-bond stacking[22] in as little as one hour of incubation in a solution of PSE suspended in methanol.[23] In this study, we explore the effect of noncovalent PSE adsorption on (5,5) SWNT bundle shearing and thus choose polyethylene to form the crosslinks because of its simple tensile behavior and lack of the side chain functionality used in other CNT/polymer composite models. We note that the choice of these specific nanotube structures and chiralities is motivated by their

successful use in previous investigations,[24,25] as well as the relatively high adsorption energy with the PSE functional group.[22] As such bundles can potentially be fabricated with many possible synthesized CNT structures, it is considered appropriate to utilize the models the authors have previously developed.

1.2 Outline

The plan of this paper is as follows. In Section 2, the computation method to construct the mesoscopic "fuzzy" nanotube model is described. Section 2.1 focuses on the coarse–grain CNT representation, while Section 2.2 describes the PSE/polyethylene crosslink coarse–grain representation. Section 2.3 describes the assembly procedure to arrive at the crosslinked bundle configuration. Section 2.4 describes the procedures of two types of tests: steered molecular dynamics (SMD) pull-out (Section 2.4.1) and displacement-control tension test (Section 2.4.2). Section 3 reports and discusses the testing results and implications of the results and the model. A summary and conclusion follows in Section 4.

2. Materials and methods

In this section we describe the derivation of the coarse–grain representations used to model the CNTs and PSE/polyethylene crosslinks. We then describe the assembly procedure of the final cross-linked bundle configuration, as well as details of the data analysis approach.

2.1 Carbon nanotube coarse–grain representation

The molecular level interactions of adjacent carbon nanotubes have been investigated using atomistic methods,[26–30] but bundles and fibers consisting of a large number of CNTs become computationally expensive at the atomistic level for relatively long carbon nanotubes or for multiple nanotubes, as the computational cost is proportional to the number of atoms in the simulation. The addition of an adhesive polymer only adds additional computational expense to full atomistic simulations. In response, mesoscopic "bead-spring" methods have proven to be a viable approach to simulate arrays of CNTs[25,31,32] and graphene.[33]

For the carbon nanotubes, a "fine-trains-coarse" multi-scale approach is implemented to produce a mesoscale model derived solely from atomistic calculations.[25,31,32] A series of full atomistic calculations of mechanical test cases (test suite) is implemented *via* classical molecular dynamics (MD) to derive a simplified set of parameters to describe the nanotube behavior. The test suite consists of the following three loading cases: (i) tensile loading, to determine Young's modulus; (ii) bending to determine the bending stiffness of CNTs; and (iii) an assembly of two CNTs to determine the adhesion energy between different nanotubes. All studies are carried out using (5,5) armchair single wall CNTs (SWCNTs) through classical molecular dynamics (albeit the method can be extended to describe CNTs with other geometry straightforwardly; but is limited here to this specific system to demonstrate the main concept and results derived from the study). For a more detailed description of the atomistic simulations and results, the reader is referred to references.[31,34] Here we provide only a brief review of the multi-scale approach. Fig. 1b depicts the molecular model of the nanotube. The MD simulations are performed using the massively parallelized modeling code LAMMPS[35] (http://lammps.sandia.gov/), capable of running on large computing clusters.

The method in deriving parameters for a mesoscale bead-type model of CNTs from the full atomistic calculation is based on a principle of energy conservation between full atomistic and coarse–grain potentials. The mesocale model is represented by a function of the total energy of the system expressed as

$$E_{\mathrm{System}} = E_{\mathrm{T}} + E_{\mathrm{B}} + E_{\mathrm{pairs}}, \tag{1}$$

where E_{T} is the energy stored in the chemical bonds due to axial stretching, E_{B} is the energy due to bending, and E_{pairs} is the energy due to weak interactions. The total energy contribution of each is calculated by a sum over all pair-wise (distance) and triple (angular) interactions in the system.

Axial stiffness. From the full atomistic results, the axial stretching behavior of carbon nanotubes is determined. We can calculate the effective Young's modulus directly *via* force–displacement results from the full atomistic simulation. For small deformation (initial stretching regime), the Young's modulus for a (5,5) single walled carbon nanotube was calculated to be approximately 2 TPa. Nonlinear behavior is neglected, as the coarse–grain simulations will be limited to small strain conditions. The total bond energy of the coarse–grain system is given by the sum over all bonded interactions, or:

$$E_{\mathrm{T}} = \sum_{\mathrm{bonds}} \phi_{\mathrm{t}}(r) \tag{2}$$

For axial stretching, a simple harmonic spring is used to determine the energy between all pairs of particles in the system, given by:

$$\phi_{\mathrm{t}}(\Delta r) = \frac{1}{2}k_{\mathrm{t}}(r - r_0)^2 = \frac{1}{2}k_{\mathrm{t}}\Delta r^2, \tag{3}$$

with k_{t} as the spring constant relating distance, r, between two particles relative to the equilibrium distance, r_0. We assume each linear regime can be approximated using the equivalent elastic strain energy and utilize the determined Young's modulus from full atomistic simulations to allow the formulation of strain energy and an equivalent k_{t}, where:

$$k_{\mathrm{t}} = \left(\frac{A_{\mathrm{c}}}{r_0}\right) Y, \tag{4}$$

with A_{c} being the cross-sectional area and Y being the determined Young's modulus. The CNT bead spacing in the reference model[31] is approximately the intertube van der Waals equilibrium distance, which can lead to hexagonal close packing of the beads within the bundle. Since the current investigation involves the direct shearing of adjacent tubes, we halve the CNT bead spacing (from the previously used equilibrium distance, r_0, of 10 Å to 5 Å) for a smoother energy landscape and scale the equivalent k_{t} accordingly. Although this smaller spacing does not prevent bead packing, test cases show that a 5 Å bead spacing eliminates significant fluctuations in shear forces to levels acceptable for this study.

Bending stiffness. For the angle potential, E_{angle}, the bending stiffness and force–displacement behavior of each structure are required. For the (5,5) single walled carbon nanotube, full

atomistic simulated bending results in a bending stiffness, EI, of 6.65×10^{-26} N m^2. The bending energy is given by a sum over all triples in the system, given by:

$$E_B = \sum_{\text{angles}} \phi_\theta(\theta). \tag{5}$$

For bending a rotational harmonic spring potential is used to determine the energy between all triples of particles in the system:

$$\phi_\theta(\theta) = \frac{1}{2} k_\theta (\theta - \theta_0)^2, \tag{6}$$

with k_θ as the spring constant relating bending angle, θ, between three particles relative to the equilibrium angle, $\theta_0 = 180°$. Again, using the equivalent elastic energy, we utilize the bending stiffness, EI, from full atomistic simulations to allow the formulation of elastic energy and an equivalent k_θ. Note that k_θ has units of energy per rad^2.

$$k_\theta = \frac{3\text{EI}}{r_0}. \tag{7}$$

Adhesion energy. We next characterize weak interactions (*i.e.* van der Waals interactions) between all pairs of coarse–grain elements, E_{pairs}. The weak interactions represent the adhesion between adjacent macromolecules, thus a full atomistic simulation with two molecules is simulated to determine the adhesion energy. The energy barrier to molecule separation (*i.e.*, the adhesion strength) and equilibrium distance can be quickly determined by minimizing the atomistic system. The geometric configuration at contact can be used to determine equilibrium distances, while the differences in energy minima between simulations at the equilibrium distance and at a semi-infinite separation can be used to extract potential energy gain of adhesion per unit length (γ_L). Here we assume a Lennard-Jones 12:6 function to represent adhesion, requiring the potential energy well depth and equilibrium distance. The total adhesion energy of the coarse–grain system is given by the sum over all pairs, or:

$$E_{\text{pairs}} = \sum_{\text{pairs}} \phi_{\text{LJ}}(r). \tag{8}$$

We use the Lennard-Jones (LJ) 12:6 function for each pair interaction:

$$\phi_{\text{LJ}}(r) = 4\varepsilon\left[\left(\frac{\sigma}{r}\right)^{12} - \left(\frac{\sigma}{r}\right)^{6}\right], \tag{9}$$

where ε describes the energy well depth at equilibrium, and σ is the distance parameter. We assume that a pair-wise interaction between different particles is sufficient to describe the adhesion between the coarse–grain elements.

The "finer-trains-coarser" approach eliminates the reliance on empirical parameter tuning. A set of mesoscopic parameters was derived from atomistic simulations using scales of femtoseconds and Angstroms. The resulting mesoscale model enables modeling of the dynamics of systems with hundreds of ultra long CNTs over time scales approaching microseconds, facilitating a bridge between atomistic theory and simulation of physical experiments. The mesoscopic model for carbon nanotubes can be defined by six parameters: k_t; r_0; k_θ; θ_0; σ; and ε. The results from the above atomistic simulations are used to determine the parameters *via* equilibrium conditions (r_0; θ_0 and σ) and energy conservation (k_t; k_θ and ε). Fig. 1b depicts the coarse–grain bead-spring model of the nanotube. All parameters are defined solely from atomistic results given in Table 1.

Table 1 Summary of mesoscopic parameters derived for (5,5) carbon nanotubes

Parameter	Units	Value
Equilibrium bead distance, r_0	Å	5.00
Tensile stiffness, k_t	kcal mol^{-1} Å^{-2}	2000.00
Equilibrium angle, θ_0	Degrees	180.00
Bending stiffness, k_θ	kcal mol^{-1} rad^{-2}	14 300.00
Dispersive parameter, ε	kcal mol^{-1}	15.10
Dispersive parameter, σ	Å	9.35

2.2 PSE–polyethylene coarse–grain representation

We introduce a generalized polymer crosslinking chain to investigate the potential to noncovalently bond CNT bundles. We consider the chains "ideal" as they represent identical polyethylene chains with no branching or defects and with symmetric PSE terminal groups. Such an ideal representation is necessary to delineate the effect of functional group density and polymer length on the mechanical behavior of the "fuzzy" CNT bundles. The coarse–grain model developed here is intended to capture two essential components of the crosslinking fibers: (1) the mechanical behavior of the polyethylene chains and (2) the intermolecular interactions between 1-Pyrenebutanoic Acid, Succinimidyl Ester (PSE) and the carbon nanotube sidewalls.

Fig. 1b depicts the atomistic model of the aromatic pyrenyl group of PSE and the polyethylene crosslink. We aim to apply a coarse–grain approach to study the mechanical behavior of a noncovalently crosslinked CNT bundle while maintaining equivalent atomistic interactions. For the PSE–polyethylene chains we again define the energy landscape of the coarse–grain system as the sum of bond, angle, and pair contributions (eqn (1)) or as a sum of the individual potentials:

$$E = \sum_{\text{bonds}} \phi_t(r_{ij}) + \sum_{\text{angles}} \phi_\theta(\theta_{ijk}) + \sum_{\text{pairs}} \phi_{\text{LJ}}(r_{ij}) \tag{10}$$

For the potentials governing the mechanical behavior of the chains (ϕ_t and ϕ_θ), parameters are defined by coarse–grain potential values of a carbon backbone chain specifically from the MARTINI force field[36] and scaled to a modified bead spacing. This approach is motivated by the fact that an underlying mechanism for crosslinks between the nanotubes is the intermolecular interactions, and not the mechanical behavior of individual carbon backbone chains. Such a generalization has been previously used in the development of coarse–grain models for lipid,[37,38] biomolecular,[39] and protein[36] systems.

For carbon chain stretching, a weak harmonic potential is implemented to govern the equivalent stretching of the polyethylene chains, given by eqn (3). For a basis, we use the parameters for the uncoiled carbon–carbon backbone bond potential from the MARTINI force field potential where $k_{cc} = 3.0$ kcal mol^{-1} Å^{-2} and $r_{cc} = 3.5$ Å. We scale the value of the carbon–carbon harmonic constant, k_{cc}, with the initial bond length, r_0, such that, $k_t(r_{cc}) = k_{cc}$,

$$k_t(r_0) = k_{cc}\left(\frac{r_{cc}}{r_0}\right) \tag{11}$$

This method treats each harmonic potential as an elastic rod with the same cross-sectional area, A, and a constant Young's modulus, E, such that the quantity, EA/r_0, is the same for all elements in the system (*i.e.* consistent stiffness of the chain). For $r_0 = 5.0$ Å, this results in $k_t = 2.1$ kcal mol^{-1} Å^{-2}. Note that for 300 K, the persistence length of unbranched polyethylene is on the order of the crosslink lengths studied here and several times the crosslink bead spacing. To capture polyethylene chain fracture, a critical stretch cutoff is appended to the harmonic potential such that $k_t = 0$ for an individual bond after that bond length. The 1.3 critical stretch value is determined by carrying out an atomistic molecular dynamics simulation of straining a C_8H_{16} polyethylene chain to failure at 0 K using ReaxFF, a first principles based reactive force field.

For bending a rotational harmonic spring potential is used to determine the energy between all triples of particles in the system, given by eqn (6). For a basis, we use the parameters for the uncoiled carbon backbone angle potential from the MARTINI force field potential where $k_{ccc} = 6.0$ kcal mol^{-1} rad^{-2}. For equivalent stiffness, we need not consider the equilibrium angles. However, we scale the value of the bending constant, k_{ccc}, with the initial length, r_0, such that

$$k_\theta(r_{cc}) = k_{ccc} \tag{12a}$$

$$k_\theta(r_0) = k_{ccc}\left(\frac{r_{cc}}{r_0}\right) \tag{12b}$$

Here, each bending potential is treated as if they had the same bending rigidity, EI, such that the quantity (EI/r_0) is the same for all elements in the system. For $r_0 = 5.0$ Å, this results in $k_\theta = 4.2$ kcal mol^{-1} rad^{-2}. The use of the harmonic potentials for both ϕ_t and ϕ_θ limits the hydrocarbon chains to small strain, which is deemed adequate for the current simulations. Fig. 1b depicts the coarse–grain bead-spring model of the crosslink.

In addition to electrostatic interactions, particles in adjacent chains interact through the LJ 12:6 potential (eqn (9)). We implement different parameters for the two bead types. For the polyethylene chain (hydrocarbon backbone), we use values of $\varepsilon = 0.8365$ kcal mol^{-1}, and $\sigma = 4.7$ Å, corresponding to apolar–apolar group interactions of the MARTINI force field.[39] For the PSE particle interactions with the carbon nanotube, we use $\varepsilon = 10.5$ kcal mol^{-1}, taken from a first principles based study of the adsorption energy of PSE with (5,5) CNT using a density functional tight-binding method.[22] For the parameter σ, we consider the equilibrium distance of PSE/(5,5) CNT of 3.05 Å,[22] and the radius of the carbon nanotube, 3.42 Å, to calculate $\sigma = 5.76$ Å. Pair potential parameters for the van der Waals interactions (Lennard-Jones 12:6) between different atom types (*i.e.* CNT–polyethylene) are mixed according to geometric means for the energy and distance terms, where:

$$\varepsilon^{AB} = \sqrt{\varepsilon^A \varepsilon^B}, \tag{13a}$$

$$\sigma^{AB} = \sqrt{\sigma^A \sigma^B}. \tag{13b}$$

A summary of the coarse–grain parameters for the PSE–polyethylene chains is given in Table 2.

Table 2 Summary of mesoscopic parameters for PSE–polyethylene chains

Parameter	Units	Value
Equilibrium bead distance, r_0	Å	5.00
Tensile stiffness, k_t	kcal mol^{-1} Å^{-2}	2.1
Equilibrium angle, θ_0	Degrees	180.00
Bending stiffness, k_θ	kcal mol^{-1} rad^{-2}	4.2
Dispersive parameter, ε		
Polyethylene–polyethylene	kcal mol^{-1}	0.8365
PSE–CNT	kcal mol^{-1}	10.5
Dispersive parameter, σ		
Polyethylene–polyethylene	Å	4.7
PSE–CNT	Å	5.8

2.3 Nanotube bundle formation

To replicate a realistic entangled carbon nanotubes/crosslink bundle, a simulated assembly procedure is motivated by the physical process of fiber extrusion. To ensure random adsorption and impregnation of crosslinks within the CNT bundle, as well as to allow variation in polymer density, the coarse–grain nanotubes are created in a parallel sheet with polymer crosslinks lying perpendicular above and below the nanotubes. The relative density of nanotubes and polymer crosslinks reflects a prepared dispersion of nanotubes and a polymer melt. To induce fiber formation, the sheet is subsequently coerced into a bundle over 0.5 ns at 300 K using a time-dependent radial external pressure, depicted in Fig. 2a, until van der Waals interactions bring the nanotubes within a final equilibrium distance. The relative speed and pressure of the bundling process can be manipulated to facilitate crosslink distribution and the homogeneity of the bundle. The CNT–PSE adsorption is assigned artificially weak during bundle formation to ensure that the bundle is more randomly crosslinked than a quasi-folded-sheet structure. When the crosslinks are in their final positions, the true CNT–PSE adsorption strength is applied, the external pressure is removed, and the bundle is equilibrated for 0.75 ns (75 000 integration steps) to a final bundle structure. The final structure is then used as the initial structure of mechanical testing and characterization, bypassing the need for assembly with each simulation.

2.4 Mechanical testing

Two distinct nanomechanical tests are performed separately on the bundles: steered molecular dynamics (SMD) pull-out simulations of a single nanotube, and displacement-control tension tests of a randomly gapped bundle. Crosslink densities and crosslink lengths are explored systematically in order to find an optimal permutation that most enhances the pull-out force, ultimate tensile stress, and modulus of toughness of a bundle.

2.4.1 Nanotube pull-out tests. The pull-out test bundle consists of 19 nanotubes, each 50 nm in length, with permutations of crosslink density and crosslink length. After bundle formation, the nanotube that is most surrounded by other nanotubes is selected to be pulled. At high crosslink densities, the interior crosslinks separate groups of nanotubes, so the pulled nanotube is not always in the center of the bundle. The end beads of the other nanotubes are fixed rigid while the pulled nanotube

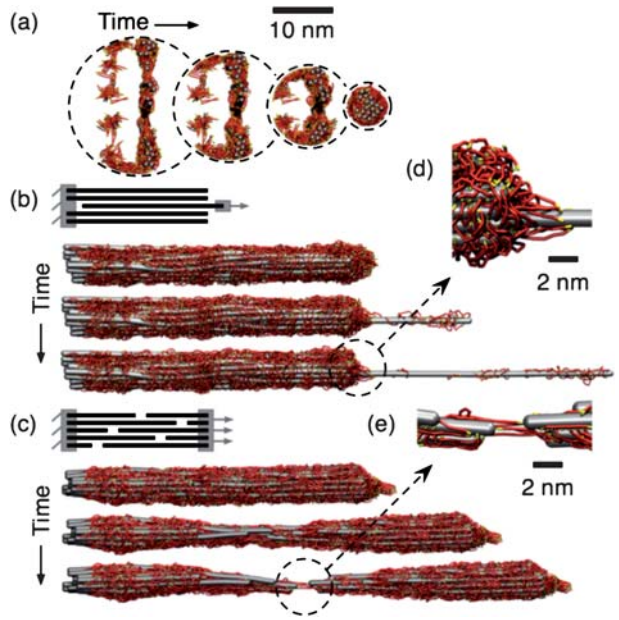

Fig. 2 CNT bundle formation and testing procedure overview. (a) First, a sheet of parallel CNTs and PSE/PE chains is relaxed into a bundle using a time-dependent radial pressure. Either a pull-out test or a tension test is then performed. (b) A pull-out test uses SMD to ramp a force on the end bead of a single nanotube. (c) A displacement-control tension test is performed by stretching the simulation box. Gaps are introduced in each nanotube so that crosslink shearing is the major failure mechanism. (d and e) By observing the crosslinks at failure points, we see that while the crosslinks are important in bridging gaps, the PSE deadsorbs before the PE is strained to failure. While PSE adsorption is not as strong as covalent intertube crosslinking, deadsorption is much more favorable than crosslink fracture in creating a damage-resistant and self-repairing bundle.

remains free. Using SMD, a harmonic spring force is applied on the end bead of the pulled nanotube and is ramped at a constant loading rate 34.8 N s^{-1} in the longitudinal direction (it is noted that in the LAMMPS molecular dynamics code, the units of force used for the simulation are kcal mol^{-1} $Å^{-1}$; the loading rate used here was set as simply 5.0 kcal mol^{-1} $Å^{-1}$ ns^{-1}, and thus the value of 34.8 N s^{-1} is a result of unit conversion). The peak force is recorded when the nanotube overcomes the PSE adsorption and intertube van der Waals interactions and is pulled completely from the bundle, as depicted in Fig. 2b. To find a reasonable loading rate, initial pull-out tests are repeated for bundles at several crosslink densities, including an uncrosslinked bundle, at both 10 times slower and 10 times faster load rates. The peak forces for each bundle permutation at these load rates are found to be within 5%, so the load rate 34.8 N s^{-1} is chosen for all pull-out tests in order to optimize data fidelity and computation efficiency.

2.4.2 Nanotube bundle tensile tests. The tension test bundles again consist of 19 nanotubes, each 50 nm in length, with permutations in crosslink density and crosslink length. After bundle formation, the end beads of each nanotube are fixed rigid. These tests explore the effects of the crosslinks on shearing of finite-length nanotubes and not on straining perfect nanotubes; therefore, a gap is introduced in each nanotube after bundle formation. Gaps are created in a random location between the rigid end regions by deleting the bonds, angles, and pair-wise interactions of two contiguous beads in each nanotube. Any energy contributions of these beads are also removed by excluding these beads from thermostat calculations. This in effect removes the beads from any interaction with the remainder of the model and separates the newly created CNT ends to avoid van der Waals interactions parallel to the tensile direction. The simulation box is stretched in the longitudinal direction, as depicted in Fig. 2c, with a constant strain rate of 50 μs^{-1}. Since the bundle ends are fixed in relation to the simulation box, scaling the simulation box is equivalent to clamping and displacing the ends of the bundle in a displacement-control tension test. The virial stress and engineering strain are recorded for a representative volumetric element (RVE) that does not include the rigid end beads or the frozen gap beads. The virial stress is commonly used to find the macroscopic (continuum) stress in molecular dynamics computations. The components of the macroscopic stress tensor, τ_{ij}, in a volume Ω are taken to be:

$$\tau_{ij} = \frac{1}{\Omega}\sum_{a\in\Omega}\left(-m^{(a)}v_i^{(a)}v_j^{(a)} + \frac{1}{2}\sum_{b\in\Omega}\left(r_i^{(a)} - r_i^{(b)}\right)F_j^{(ab)}\right) \qquad (14)$$

where $m^{(a)}$ is the mass of atom "a", $v_i^{(a)}$ and $v_j^{(a)}$ are the velocities in the ith and j^{th} vector component basis, $r_i^{(a)} - r_i^{(b)}$ denotes the distance between atom "a" and atom "b" along the ith vector component, while $F_j^{(ab)}$ is the force on atom "a" exerted by atom "b" along the jth vector component, and Ω is the volume. To reduce random and temperature-related stress fluctuations, in addition to averaging over the representative volume, Ω, the stress is averaged further over a small time interval of 125 ps around the desired time of the stress.

To compute the representative volume (and associated stress), the cross-sectional area of each bundle is estimated by drawing a closed spline around a transverse slice through the undeformed bundle. For the tension test bundle consisting of nineteen (5,5) uncrosslinked nanotubes, the bare bundle cross-sectional area is 16.44 nm^2. The visualized transverse slice areas are shown normalized to the bare bundle area in Fig. 3b. To compute the modulus of toughness U_t, the stress is integrated from 0 to 1 engineering strain.

After the effects of crosslink density variations are explored, we investigate the contributions of adsorption strength and crosslink stiffness. Starting from the formed bundle structure of each crosslink length permutation at 20 wt%, the bundles are equilibrated further after assigning artificially strong crosslink end adsorption by modifying the Lennard-Jones dispersive parameter ε; higher crosslink stiffness by modifying the PE chain spring constant k; or combinations thereof. The tensile test is then repeated using these modified parameters.

3. Results and discussion

We begin our analysis by focusing on the force required to pull a single nanotube from a bundle with permutations of crosslink length and crosslink density by carrying out a series of computational experiments. Generally, we find that the critical pull-out force (defined in Fig. 4a) increases with crosslink density for the crosslink lengths considered. For each crosslink length, the

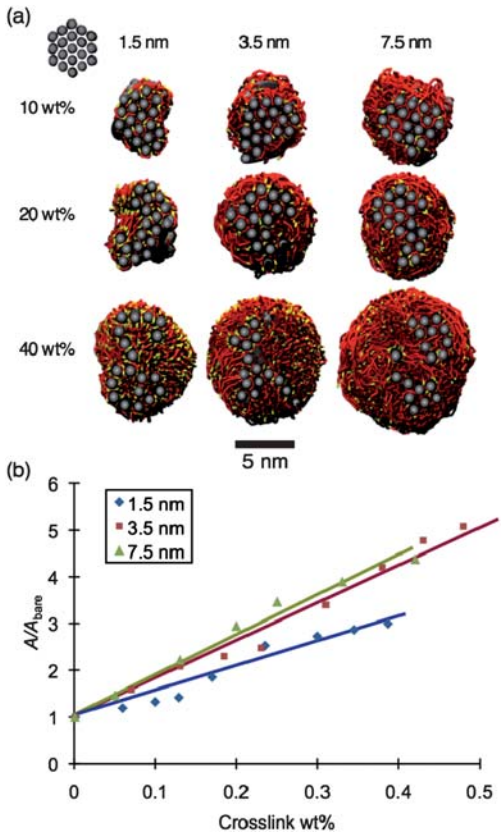

Fig. 3 Examples of transverse bundle slices used to estimate cross-sectional area for virial stress calculations. As the crosslink density increases, CNTs are spread apart by the crosslink impregnation inherent in the bundle formation process. PSE adsorption during bundling prevents the crosslinked bundles from forming a perfect hexagonal bundle, as in the uncrosslinked bundle in the upper-left corner.

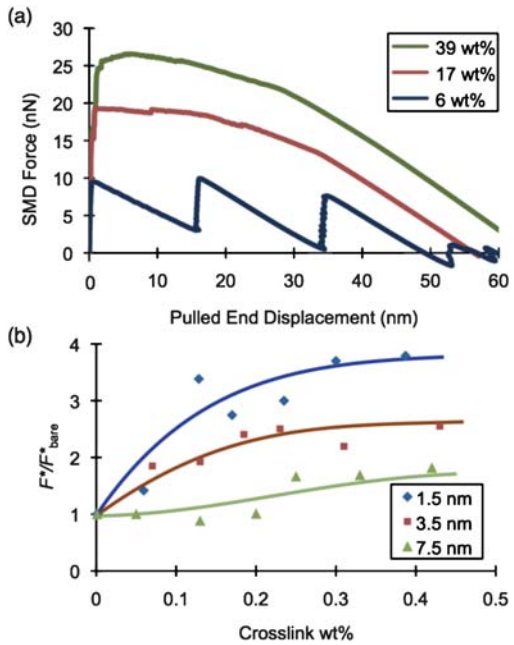

Fig. 4 Pull-out tests carried out using SMD to ramp a force on a single nanotube until it slips from the bundle. (a) Examples of force/displacement curves, here for 1.5 nm crosslinks, show the nanotube slipping at a critical pull-out force F^*. The slip–stick behavior of crosslink densities below 17 wt% is consistent for all tested crosslink lengths and is lost at faster load rates. (b) The critical slipping force F^* is plotted normalized to the slipping force F^*_{bare} of the uncrosslinked bundle. At a given crosslink density, shorter crosslinks require a higher pull-out force. For each crosslink length, the pull-out force saturates above 20 wt% crosslink density.

critical pull-out force can be fitted to the crosslink density by a power law relationship, as presented in Fig. 4b. With this power law relationship, we find a saturation regime in which the pull-out force increases negligibly for crosslink densities above 20 wt%. During synthesis of these bundles, a crosslink density of 20% may be optimal in order to conserve the amount of PSE used. We also find that the critical pull-out force decreases with crosslink length. For example, at ~40 wt%, the bundle with shorter 1.5 nm crosslinks shows a pullout force enhancement (*i.e.*, F^*/F^*_{bare}) about twice that of the bundle with longer 7.5 nm crosslinks.

We now test the crosslink saturation predictions against a tension test of the bundle, illustrated in Fig. 2c, in which we focus on the peak virial stress within a representative volumetric element (RVE). The stress–strain responses show an elastic regime with a Young's modulus between 300 and 400 GPa, then a pseudo-plastic regime dependent on the remaining CNT overlapping length. The maximum virial stress σ^* in the bundle is normalized by the σ^*_{bare} in a bare (*i.e.* uncrosslinked) bundle. Examples of stress/strain curves of bundles with 1.5 nm crosslinks are shown in Fig. 5a. The maximum stress condition at a stress level of σ^* occurs with less than 5% strain, but a bundle stress is maintained until 80% strain because the crosslinks can repeatedly adsorb even after large bundle deformation. Normalized virial stress, plotted in Fig. 5b, indicates that stronger bundles are achieved using shorter 1.5 nm crosslinks, with a maximum enhancement of $\sigma^*/\sigma^*_{bare} = 4.2$ for 1.5 nm crosslinks at 17 wt%. However, strength enhancement decreases with crosslink densities greater than 20 wt%, which agrees with the saturation regime found in the pull-out tests. Intermediate 3.5 nm crosslinks show a similar maximum at 22 wt%, but with only $\sigma^*/\sigma^*_{bare} = 2.4$. Longer 7.5 nm crosslinks enhance the bundle stress under $\sigma^*/\sigma^*_{bare} = 1.4$. Normalized modulus of toughness U_t, plotted in Fig. 5c, shows similar enhancements of up to $U_t/U_{t,bare} = 5.4$ for 1.5 nm crosslinks at 17% and $U_t/U_{t,bare} = 4.3$ with 3.5 nm crosslinks at 23 wt%. Longer 7.5 nm crosslinks enhance the modulus of toughness under $U_t/U_{t,bare} = 2.6$. It is important to note that longer bundles with multiple gaps along each CNT may exhibit more complex deformation behaviors. Normalized virial stress and normalized modulus of toughness are plotted over one another in Fig. 6, in the spirit of Ashby-plots. These data show the narrow range of crosslink density that achieves such enhanced bundle properties, that is, the combination of both high strength and high toughness.

Through visual inspection of transverse slices of each bundle, it is observed that the CNTs are spread apart by the crosslinks due to the impregnation inherent in the bundle formation process. Examples of 10, 20, and 40 wt% are shown in Fig. 3a. Adsorption of PSE during bundle formation prevents the

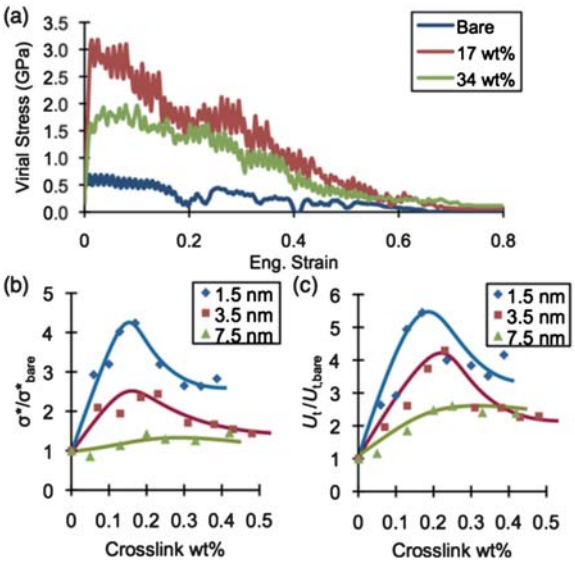

Fig. 5 Displacement-controlled tension test results. (a) Examples of stress/strain curves with 1.5 nm crosslinks. (b) The maximum virial stress σ^* in the bundle is normalized by σ^*_{bare} in a bare (*i.e.* uncrosslinked) bundle. The strongest bundles are achieved using shorter 1.5 nm crosslinks with a maximum enhancement of $\sigma^*/\sigma^*_{bare} = 4.2$ at 17 wt%. (c) The modulus of toughness U_t is normalized by $U_{t,bare}$ in a bare bundle and shows a similar saturation behavior above 20 wt%.

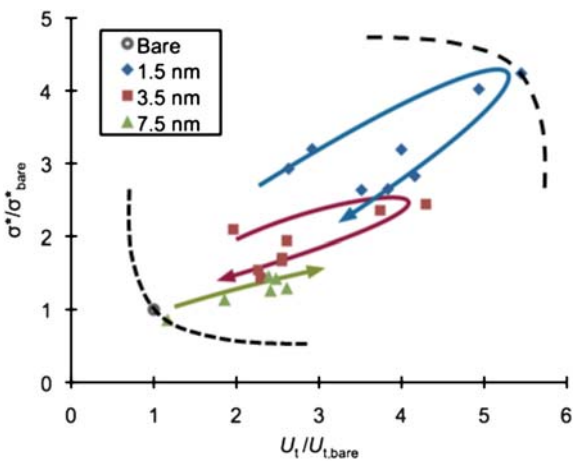

Fig. 6 Ashby-plot of the normalized strength *versus* toughness shows that certain material parameters provide the structural basis for both high strength and high toughness. The crosslink permutation that optimizes both strength and toughness is 1.5 nm length crosslinks at 17 wt%. The arrows show the direction of increasing crosslink density. For the same strength enhancement, tougher bundles can be achieved using higher crosslink densities. This result demonstrates that the material has the capacity to combine disparate material properties, providing a structural basis for the inverse banana-curve behavior (wide dashed line). This is in contrast to the properties of many engineered materials, which show a banana-curve behavior (narrow dashed line) where high strength is achieved on the expense of high toughness.

crosslinked bundles from forming the hexagonal packing of an uncrosslinked bundle. The CNT disorder in the crosslinked bundles causes initial bending and straining of the CNTs. This in turn causes an initial virial stress before testing, and this initial stress increases with crosslink density. Since CNTs are visually spread apart at crosslink densities above 20 wt%, it is predicted that a critical crosslink density exists in which CNTs slide more against the polyethylene chains than against other CNTs. Evidence for this transition can be seen in the slip–stick behavior of bundles with crosslink densities below 13 wt% for the pull-out tests. Exemplary force–displacement curves are shown in Fig. 4a for bundles with 1.5 nm crosslinks. The 6 wt% bundle shows an initial slip at 9.5 nN, reloading until it slips again at 10 nN, and another reloading until it slips again at 7.5 nN. In contrast, bundles with crosslink densities greater than 17 wt% show no sticking after the initial slip, even at slower load rates. This transition is consistent for all tested crosslink lengths. Further evidence for this transition is seen in the saturation regime of the tension test peak stresses at the same critical crosslink density. The peak virial stress σ^* decreases drastically for crosslink densities greater than 17 wt% with 1.5 nm crosslinks and 23 wt% with 3.5 nm crosslinks.

Two potential toughening mechanisms are observed: crosslink straightening and gap bridging. These mechanisms are depicted for bundles with 20 wt% crosslink density in Fig. 7. Crosslink straightening in the gap wake is physical evidence of PE chain loading and is a chief energy release mechanism during the tension test. After bundle formation, the polyethylene chains of the crosslinks are initially coiled around CNTs. As the CNTs are sheared during tensile loading of a gapped bundle, the polyethylene chains that crosslink the nanotubes are loaded in the opposite direction and are pulled straight and are eventually directly loaded. When these loaded crosslinks reach a critical tensile condition, the PSE de-adsorbs before the polyethylene fractures, and the crosslink is left straightened and intact in the gap wake. Other crosslinks along the bundle are then loaded, straightened, and de-adsorbed until there is no more overlap between the two bundle ends. At the moment of no overlap, we still see crosslinking of the two bundle ends. While shorter crosslinks give stronger bundles, long crosslinks may be more

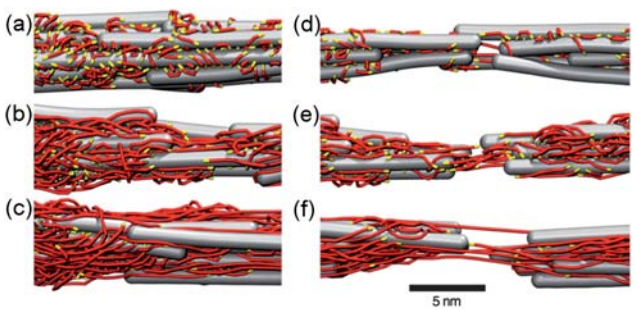

Fig. 7 Crosslink straightening (left) and gap bridging (right) contribute to high toughness. Crosslink straightening in the gap wake, shown here for bundles with (a) 1.5 nm, (b) 3.5 nm, and (c) 7.5 nm crosslinks at 20 wt%, is physical evidence of PE chain loading and a chief energy release mechanism during the tension test. PSE deadsorbs before the PE fractures, and the crosslink is left straightened in the gap wake. At the moment of no overlap, we still see crosslinks bridging the separated bundle pieces, shown here for bundles with (d) 1.5 nm, (e) 3.5 nm, and (f) 7.5 nm crosslinks at 20 wt%. While shorter crosslinks give stronger bundles, long crosslinks may be more useful in crack bridging and self-repair mechanisms.

useful in crack bridging and self-repair mechanisms at a higher hierarchical level than is studied here.

The "fuzzy" wood-inspired model exhibits large-scale shearing behavior similar to wood cells and hook-and-loop fasteners. To observe this behavior, the gapped-bundle tension test is repeated with a relaxation period in which one end of the bundle is free to move for 5 ns, then reloaded. The virial stress is plotted for bundles with 20 wt% crosslink density in Fig. 8. Stress is plotted against simulation time instead of strain in order to clearly show the relaxation period. For all cases, the virial stress returns to the stress value directly preceding relaxation, just as is found in wood foils.[16] However, stress during relaxation depends on the cross-link length; for bundles with 7.5 nm crosslinks, the relaxed stress is very close to the original, finite bundle stress. (Note that the initial bundle stress is finite even after equilibration because the crosslinks are kept deformed due to the PSE adsorption.) In contrast, bundles with 1.5 nm crosslinks exhibit a relaxed stress equal to the stress directly preceding relaxation. Shorter cross-links lock adjacent CNTs in a deformed position, while longer crosslinks allow adjacent CNTs to translate during relaxation.

For cases with artificially stronger crosslink end adsorption, polyethylene chain fracture rather than PSE de-adsorption becomes the dominant mode of crosslink deformation. Therefore, the atomistically derived 30% critical strain is used in the polyethylene chain potential in order to capture the chain fracture, shown in Fig. 9. Again, shorter 1.5 nm crosslinks allow much stronger bundles, and the difference becomes greater at stronger crosslink end adsorptions. Increasing the crosslink end adsorption strength is a much more dominant factor in σ^* than crosslink stiffness. For example, with 1.5 nm crosslinks, a 10-fold increase in adsorption strength leads to peak stress 45 times greater than a bare bundle. Therefore, further research should focus on noncovalent crosslink functionalizing molecules similar to PSE rather than on polymer chain chemistry for these kinds of polymer-reinforced CNT bundles.

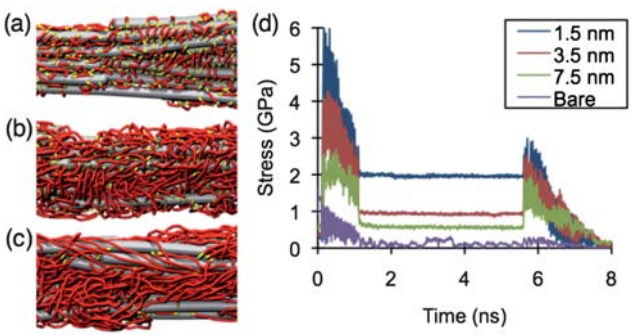

Fig. 8 Residual strength in plastically deformed bundles with a relaxation period. (a) 1.5 nm crosslinks immediately lock adjacent CNTs in a deformed position. (b) As the tests are repeated with longer crosslinks (here, 3.5 nm), the bundle has greater degrees of freedom with which to relax. (c) 7.5 nm crosslinks allow the bundle to relax enough to bring the virial stress to the pre-strained value. (d) We see these effects clearly when the virial stress is plotted for bundles with these crosslink lengths at 20 wt% crosslink density. Here, stress is plotted against simulation time instead of strain in order to clearly show the relaxation period. For all cases, the virial stress upon reloading returns to the stress value directly preceding relaxation, confirming a shearing behavior similar to wood.

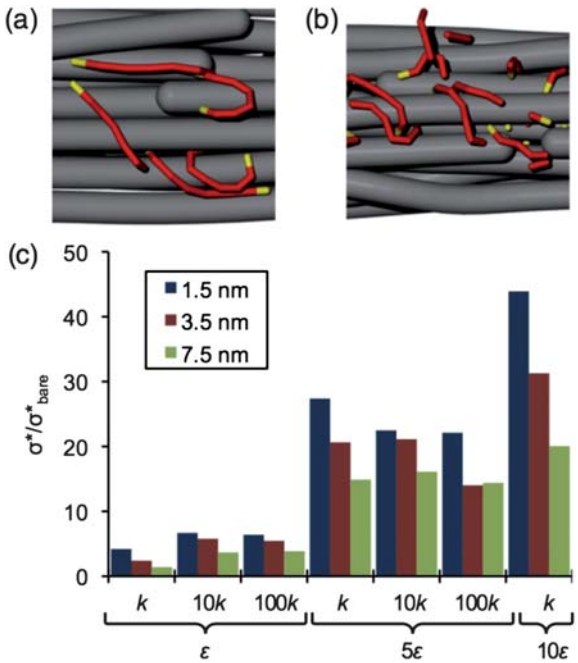

Fig. 9 Exploration of adsorption and crosslink stiffness stress contribution. Tension tests are repeated with artificially strong crosslink end adsorption. (a) Under normal conditions, PSE deadsorbs before the PE chain is strained to failure. (b) For cases with artificially stronger cross-link end adsorption, PE chain fracture becomes the dominant mode of crosslink deformation. (c) The virial stress improvement σ^*/σ^*_{bare} is plotted for 20 wt% bundles. Shorter 1.5 nm crosslinks create much stronger bundles, and the difference becomes greater at stronger crosslink end adsorptions. Increasing the crosslink end adsorption strength is a much more dominant factor in σ^* than crosslink stiffness.

4. Conclusions

Using a coarse–grain model of CNTs and a disordered polymer phase, we explored the effects of noncovalently adsorbing crosslinks in the improvement of CNT bundle properties for the eventual development of viable polymer-reinforced CNT fibres or composites as a novel engineering material. Pull-out tests and bundle tension tests show that shorter crosslinks are more beneficial to bundle strength, and a crosslink density of approximately 20 wt% is best for the small bundles studied here. Our results demonstrate that certain combinations of cross-link lengths and densities provide the capacity for combinations of extreme toughness at extreme strength (Fig. 6). The quantitative analysis of our data suggests that this optimal behavior is reached for 1.5 nm long crosslinks at 17 wt% density. This finding suggests that, similar to many biological materials, structural arrangements exist that enable us to combine disparate material properties through the design of appropriate nanostructures.

The model proposed here can be modified to explore other noncovalent crosslinking as reinforcement in bundles, including systems made of a greater number of nanotubes, nanotubes of larger diameters, and even combinations of single- and multi-walled nanotubes.[40] While shorter crosslinks create stronger bundles at the length scale studied in this paper, longer crosslinks may increase bulk toughness by bridging cracks, but much larger length scales would have to be studied, suggesting that such

additional hierarchical features may be important for mechanical properties. Layer deposition of the initial parallel sheet structure (instead of bundle formation used here) could also be used to study buckypaper reinforcement. By varying the crosslink length and adsorption strength, many other polymers can be explored as reinforcing agents; especially of interest would be long polymer chains with many adsorbing side chains along its length instead of the short chains presented in this paper. With further atomistic study, future models may explore the end-to-end functionalization of finite-length nanotubes to create a long bundle with the damage-resistant properties of spider silk.

Acknowledgements

We acknowledge support from the ARO-MURI program (Award No. W911NF-09-1-0541) funded by DoD.

References

1 R. H. Baughman, A. A. Zakhidov and W. A. de Heer, Carbon nanotubes—the route toward applications, *Science*, 2002, **297**, 787–792.
2 M. M. J. Treacy, T. W. Ebbesen and J. M. Gibson, Exceptionally high Young's modulus observed for individual carbon nanotubes, *Nature*, 1996, **381**, 678–680.
3 F. Li, et al., Tensile strength of single-walled carbon nanotubes directly measured from their macroscopic ropes, *Appl. Phys. Lett.*, 2000, **77**(20), 3161–3163.
4 P. M. Ajayan and F. Banhart, Strong bundles, *Nat. Mater.*, 2002, **3**, 135–136.
5 A. Kis, et al., Reinforcement of single-walled carbon nanotube bundles by intertube bridging, *Nat. Mater.*, 2004, **3**, 153–157.
6 A. B. Dalton, et al., Super-tough carbon-nanotube fibers, *Nature*, 2003, **423**, 703.
7 H. W. Zhu, et al., Direct synthesis of long single-walled carbon nanotube Strands, *Science*, 2002, **296**, 884–886.
8 D.-C. Li, et al., Structure and growth of aligned carbon nanotube films by pyrolysis, *Chem. Phys. Lett.*, 2000, **316**, 349–355.
9 X. Liu, K. H. R. Baronian and A. Downard, Patterned arrays of vertically aligned carbon nanotube microelectrodes on carbon films prepared by thermal chemical vapor deposition, *Anal. Chem.*, 2008, **80**, 8835–8839.
10 Q. Zhang, et al., Radial growth of vertically aligned carbon nanotube arrays from ethylene on ceramic spheres, *Carbon*, 2008, **46**(8), 1152–1158.
11 E. J. Garcia, et al., Fabrication and multifunctional properties of a hybrid laminate with aligned carbon nanotubes grown *in situ*, *Compos. Sci. Technol.*, 2008, **68**(9), 2034–2041.
12 B. L. Wardle, et al., Fabrication and characterization of ultrahigh-volume-fraction aligned carbon nanotube–polymer composites, *Adv. Mater.*, 2008, **20**(14), 2707–2714.
13 H. Qian, et al., Carbon nanotube-based hierarchical composites: a review, *J. Mater. Chem.*, 2010, **20**(23), 4751–4762.
14 B. Brushan, Biomimetics: lessons from nature—an overview, *Philos. Trans. R. Soc. London, Ser. A*, 2009, **367**, 1445–1486.
15 R. O. Ritchie, M. J. Buehler and P. Hansma, Plasticity and toughness in bone, *Phys. Today*, 2009, **62**(6), 41–47.
16 P. Fratzl and R. Weinkamer, Nature's hierarchical materials, *Prog. Mater. Sci.*, 2007, **52**, 1263–1334.
17 K. Mylvaganam and L. C. Zhang, Chemical bonding in polyethylene–nanotube composites: a quantum mechanics prediction, *J. Phys. Chem. B*, 2004, **108**(17), 5217–5220.
18 Y.-C. Liu, et al., Diffusion dynamics of water controlled by topology of potential energy surface inside carbon nanotubes, *Phys. Rev. B: Condens. Matter Mater. Phys.*, 2008, **77**(12), 125438.
19 S. J. V. Frankland, et al., Molecular simulation of the influence of chemical cross-links on the shear strength of carbon nanotube–polymer interfaces, *J. Phys. Chem. B*, 2002, **106**(12), 3046–3048.
20 E. J. Wallace and M. S. P. Sansom, Carbon nanotube/detergent interactions *via* coarse-grained molecular dynamics, *Nano Lett.*, 2007, **7**(7), 1923–1928.
21 P. Angelikopoulos, S. Al Harthy and H. Bock, Structural forces from directed self-assembly, *J. Phys. Chem. B*, 2009, **113**(42), 13817–13824.
22 W. Fan and R. Zhang, Structural and electronic properties of single-walled carbon nanotubes adsorbed with 1-pyrenebutanoic acid, succinimidyl ester, *Sci. China, Ser. B: Chem.*, 2008, **51**(12), 1203–1210.
23 R. J. Chen, et al., Noncovalent sidewall functionalization of single-walled carbon nanotubes for protein immobilization, *J. Am. Chem. Soc.*, 2001, **123**(16), 3838–3839.
24 M. J. Buehler, Mesoscale modeling of mechanics of carbon nanotubes: self-assembly, self-folding, and fracture, *J. Mater. Res.*, 2006, **21**(11), 2855–2869.
25 S. Cranford and M. J. Buehler, Mechanomutable carbon nanotube arrays, *Int. J. Mater. Struct. Integr.*, 2009, **3**(2/3), 161–178.
26 B. Chen, et al., Binding energy of parallel carbon nanotubes, *Appl. Phys. Lett.*, 2003, **83**(17), 3570–3571.
27 K. M. Liew, C. H. Wong and M. J. Tan, Buckling properties of carbon nanotubes, *Appl. Phys. Lett.*, 2005, **87**(4), 041901.
28 K. M. Liew, C. H. Wong and M. J. Tan, Tensile and compressive properties of carbon nanotube bundles, *Acta Mater.*, 2006, **54**, 225–231.
29 W. Zhou, et al., Self-folding of single- and multiwall carbon nanotubes, *Appl. Phys. Lett.*, 2007, **90**, 073107.
30 C. Zhu, Z. Xie and K. Guo, Formation of close-packed multi-wall carbon nanotube bundles, *Diamond Relat. Mater.*, 2004, **13**, 180–183.
31 M. J. Buehler, A. C. T. v. Duin and W. A. Goddard, Multi-paradigm modeling of dynamical crack propagation in silicon using the ReaxFF reactive force field, *Phys. Rev. Lett.*, 2006, **96**(9), 095505.
32 S. Cranford, et al., A single degree of freedom 'lollipop' model for carbon nanotube bundle formation, *J. Mech. Phys. Solids*, 2009, **58**(3), 409–427.
33 S. Cranford, D. Sen and M. J. Buehler, Meso-origami: folding multilayer graphene sheets, *Appl. Phys. Lett.*, 2009, **95**(12), 123121.
34 S. Cranford and M. Buehler, *In silico* assembly and nanomechanical characterization of carbon nanotube buckypaper, *Nanotechnology*, 2010, **21**(26), 265706.
35 S. J. Plimpton, Fast parallel algorithms for short-range molecular dynamics, *J. Comput. Phys.*, 1995, **117**, 1–19.
36 L. Monticelli, et al., The MARTINI coarse-grained force field: extension to proteins, *J. Chem. Theory Comput.*, 2008, **4**, 819–834.
37 J. C. Shelley, et al., Simulations of phospholipids using a coarse–grain model, *J. Phys. Chem. B*, 2001, **105**, 9785–9792.
38 S. J. Marrink, A. H. de Vries and A. E. Mark, Coarse grained model for semiquantitative lipid simulations, *J. Phys. Chem. B*, 2004, **108**, 750–760.
39 S. J. Marrink, et al., The MARTINI force filed: coarse grained model for biomolecular structures, *J. Phys. Chem. B*, 2007, **111**, 7812–7824.
40 B. Ping, M. Locascio, P. Zapol, S. Li, S. Mielke, G. Schatz and H. D. Espinosa, Measurements of near-ultimate strength for multiwalled carbon nanotubes and irradiation-induced crosslinking improvements, *Nat. Nanotechnol.*, 2008, **3**(10), 626–631.

